ELSEVIER

Contents lists available at ScienceDirect

International Journal of Refractory Metals and Hard Materials

journal homepage: www.elsevier.com/locate/IJRMHM





High-temperature mechanical properties and oxidation behavior of Hf-27Ta and Hf-21Ta-21X (X is Nb, Mo or W) alloys

O.N. Senkov^{a,b,*}, T.I. Daboiku^{a,b}, T.M. Butler^a, M.S. Titus^c, N.R. Philips^d, E.J. Payton^a

- ^a Air Force Research Laboratory, Materials and Manufacturing Directorate, Wright-Patterson AFB, OH 45433, USA
- ^b UES, Inc., 4401 Dayton-Xenia Rd., Dayton, OH 45432, USA
- ^c School of Materials Engineering, Purdue University, West Lafayette, IN 47907, USA
- d ATI Specialty Alloys and Components, Albany, OR 97321, USA

ARTICLE INFO

Keywords: Hafnium-based refractory alloys Microstructure Mechanical properties Oxidation

ABSTRACT

The microstructure, mechanical properties (at 25 °C, 1000 °C, 1200 °C, 1400 °C and 1600 °C) and oxidation behavior (at 1600 °C) of a binary Hf-27%Ta alloy and three ternary alloys, Hf-21%Mo-21%Ta, Hf-21%Nb-21%Ta and Hf-21%Ta-21%W (compositions are in atomic percent) are reported. The alloys were produced by vacuum arc melting, hot isostatically pressed under a high-purity argon pressure of 207 MPa at 1400 °C for 3 h and slow cooled to room temperature. The Hf-27Ta alloy had a microstructure consisting of coarse primary HCP particles and a monotectoidally transformed matrix consisting of a nano-lamellar mixture of the Ta-rich BCC and Hf-rich HCP phases. The Hf-21Mo-21Ta alloy consisted of a BCC matrix phase and HCP precipitates. Hf-21Nb-21Ta had a microstructure consisting of a BCC matrix phase, spherical nano-precipitates inside the matrix grains and twophase BCC lamellar regions at grain boundaries, with no HCP phase detected. The Hf-21Ta-21W alloy had a three-phase structure consisting of a Hf-rich HCP matrix, W-rich cubic Laves phase and monotectoidally transformed regions consisting of nano-lamellae of Ta-rich BCC and Hf-rich HCP phases. The alloys had limited ductility at room temperature but they all were well workable at $T \ge 1000$ °C. Among the studied alloys, the binary Hf-27Ta was the strongest at room temperature and the Hf-21Mo-21Ta was the strongest at high temperatures. The oxidation kinetics of Hf-27Ta, Hf-21Mo-21Ta and Hf-21 W-21Ta were similar, with 30-40 mg/ cm² mass gain per 1 h holding at 1600 °C. The Hf-21Nb-21Ta alloy exhibited much higher (~230 mg/cm²/h) mass gains at 1600 °C. The ternary alloys all showed evidence of the formation of gaseous and/or liquid species in the oxide scales.

1. Introduction

Refractory alloys have attractive properties, such as high melting temperature above ${\sim}1800~^{\circ}\text{C}$, good creep resistance, high thermal conductivity and low thermal expansion, which make them potential candidates for high-temperature structural applications beyond advanced Ni-based superalloys [1,2]. Ni-based superalloys have been considered for many decades as the best materials for use in heavy loading structures operating at temperatures up to 1000 $^{\circ}\text{C}$, such as turbine engine disks and blades. However, the maximum use temperatures of Ni superalloys are now reaching their limits due to rapid softening when the temperature approaches their relatively low melting temperatures (${\sim}1250{-}1400~^{\circ}\text{C}$). Considerably higher melting temperatures of refractory alloys can extend engine operating temperatures

much beyond 1000 °C. The main drawback of refractory alloys, which limits their use at high temperature, is poor oxidation resistance, and protective coatings are required. Even when oxidation resistant coatings are used, there is concern of failure because any local degradation of the protective coating will cause rapid oxidation and failure of the structure. Therefore, development of refractory alloys with improved oxidation resistance is needed.

Early publications by Marnoch [3,4] reported enhancing oxidation resistance of binary Hf-Ta alloys with the compositions close to 27 wt% (26.7 at.%). Recently, Perepezko [5] and Yang et al. [6] confirmed this finding and found out that the superior oxidation resistance of the Hf-Ta binary alloys at temperatures up to $1600\,^{\circ}\mathrm{C}$ is caused by the formation of a stable Hf₆Ta₂O₁₇ oxide scale. This scale adheres well with the alloy substrate and is thermal shock resistant. With this observation and the

^{*} Corresponding author at: Air Force Research Laboratory, Materials and Manufacturing Directorate, Wright-Patterson AFB, OH 45433, USA. *E-mail address:* oleg.senkov.ctr@us.af.mil (O.N. Senkov).

Table 1 The density $(\rho, \text{ in g/cm}^3)$ and chemical composition (in at.%) of the studied alloys.

Alloy ID	ρ	Hf	Ta	Mo	Nb	W	O	N	С
Hf-Ta	13.79 ± 0.01	71.6	28.0				0.112	0.127	0.149
Hf-Nb-Ta	13.11 ± 0.02	56.5	22.7		20.6		0.020	0.023	0.121
Hf-Mo-Ta	13.62 ± 0.01	56.3	22.9	20.5			0.040	0.150	0.094
Hf-Ta-W	14.83 ± 0.03	57.4	21.7			20.8	0.011	< 0.026	0.105

identified reaction pathway, the diffusion of oxygen through the scale was concluded to be the rate-limiting factor for the oxidation of these binary alloys [6].

It can be also noted that the alloys of the Hf-Ta system form carbides with very high melting points, exceeding 3900 $^{\circ}$ C [7], and recently non-stochiometric hafnium carbonitrides with the melting points exceeding 4000 $^{\circ}$ C were reported [8]. The Hf-Ta carbides were found to have low

vaporization rates and high thermal stability at temperatures up to 2275 $^{\circ}\text{C}$ [9]. Similar to Hf-Ta alloys, the Hf-Ta carbides have good oxidation resistance at temperatures up to 1600 $^{\circ}\text{C}$ by forming a Hf₆Ta₂O₁₇ protective layer [10]. The outlined results indicate that the Hf-Ta system can be a basis for the development of high-temperature refractory materials for operation at temperatures much beyond 1000 $^{\circ}\text{C}$. Unfortunately, there is very limited information in the open

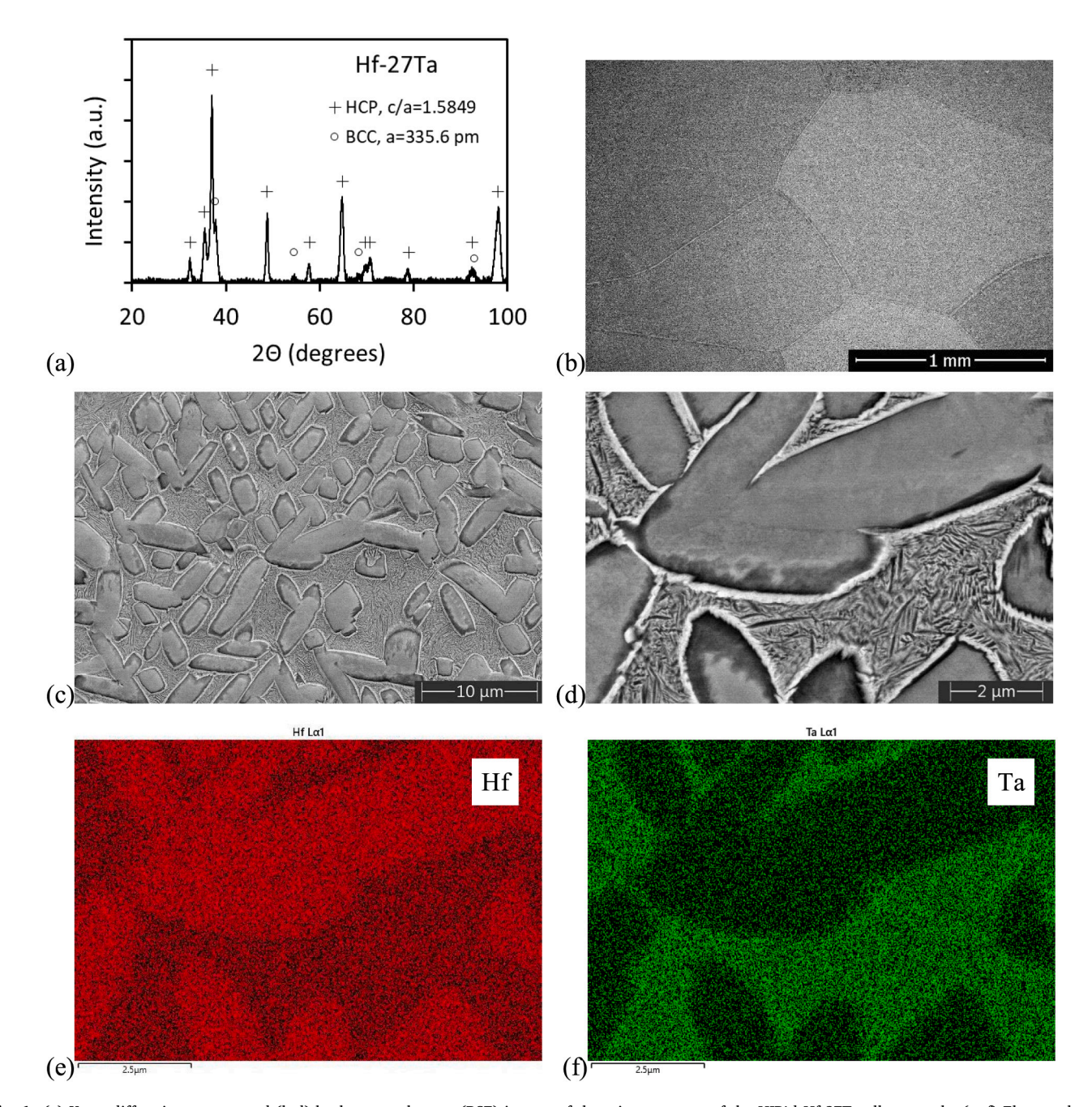


Fig. 1. (a) X-ray diffraction pattern and (b-d) backscatter electron (BSE) images of the microstructure of the HIP'd Hf-27Ta alloy sample. (e, f) Elemental maps showing distributions of (e) Hf and (f) Ta inside the alloy constituents shown in figure (d).

literature on high-temperature mechanical properties and on the effect of a third alloying element on the microstructure, oxidation behavior and mechanical properties of the Hf-Ta alloys.

In this work we report the microstructure, high-temperature mechanical properties and oxidation behavior of a binary Hf-27Ta alloy and three ternary alloys, Hf-21Mo-21Ta, Hf-21Nb-21Ta and Hf-21Ta-21W. These three ternary alloys maintain a Ta to Hf ratio similar the binary alloy showing the best oxidation resistance.

2. Experimental procedures

One binary alloy, Hf-27Ta, and three ternary alloys, Hf-21Ta-21X, where X = Nb, Mo, or W and the compositions are given in at. %, were prepared by vacuum arc melting of high purity (>99.95%) elements. Each alloy button (weighing 150 g) was mixed and melted inside a water-cooled copper cavity. In order to achieve homogeneity in the liquid state, each alloy was melted, held in the molten state for $\sim\!30$ s under active mixing by the arc and cooled down. The alloys were flipped over and re-melted at least 5 times. After the final solidification inside the water-cooled copper cavity, the alloys were wrapped in Ta foil and hot isostatic pressed (HIP'd) at 1400 °C under 207 MPa pressure of high purity argon for 3 h. The heating and cooling rates were 15 °C per minute. The average alloy compositions were measured using direct current plasma atomic emission spectrometry (metals), inert gas fusion (oxygen and nitrogen) and combustion infrared absorption (carbon) methods, and the measurements are given in Table 1.

Microstructure, local chemical compositions and crystal structures were studied using a field emission scanning electron microscope (FEG-SEM) equipped with backscatter electron (BSE), energy dispersive spectroscopy (EDS) and electron backscatter diffraction (EBSD) detectors. The reported chemical compositions of different alloy constituents are the average values of at least 10 measurements made from different locations. The volume/area fractions of secondary phases were measured on BSE images using Adobe Photoshop ad-ins allowing segmentation and measurements of the areas with different gray color. Xray diffraction (XRD) was conducted using Cu-K $_{\alpha 1}$ radiation in the 2θ range of 10° to 120°. Prior to microscopy, specimens were mounted in a conductive phenolic resin and polished using conventional metallographic techniques. Pandat_2020 software together with PanSolution-2020 thermodynamic database [11,12] and ThermoCalc software together with TCHEA-4 thermodynamic database [13] were used to calculate phase diagrams.

The alloy densities were measured using a helium pycnometer and the results are given in Table 1. Vickers microhardness testing was conducted using a square-based diamond pyramid by applying a 1000 g load for 15 s to a flat, polished surface of the alloy samples. Isothermal compression mechanical tests were conducted at 25 °C, 1000 °C, $1200~^{\circ}\text{C}$, $1400~^{\circ}\text{C}$ and $1600~^{\circ}\text{C}$ at a constant ram speed of 0.0075~mm/sthat corresponded to an initial strain rate of 0.001 s⁻¹. Compression specimens had a square cross-section of 4.6 mm \times 4.6 mm and the height of 7.5 mm. Room temperature tests were conducted in air and high-temperature tests were conducted in vacuum of $\sim 2 \times 10^{-3}$ Pa. A more detailed description of the compression tests can be found elsewhere [14]. Oxidation testing was conducted on samples with the same geometry. Prior to oxidation testing, specimens were ground to 600 grit and cleaned with acetone followed by isopropanol. Specimens were weighed before and after oxidation using a high sensitivity scale (10^{-5} g) and the weight gain compared on the basis of original sample surface areas (e.g. mg/cm²). All oxidized specimens were encapsulated in cold epoxy to preserve the oxide scales prior to sectioning and polishing.

3. Results and discussion

3.1. Microstructure of a Hf-27Ta binary alloy

X-ray diffraction of the Hf-27%Ta alloy identifies diffraction peaks

Table 2 Volume fraction (V_t) and chemical compositions (in at.%) of different constituents in the Hf-27Ta alloy, as determined by SEM/EDS and calculated at 1100 °C.

Element	Vf	Hf	Ta	
Experiment				
Whole area (Fig. 1c)	1	$\textbf{74.5} \pm \textbf{0.4}$	25.5 ± 0.4	
Ta-rich areas	0.65	62.1	37.9	
Hf-rich particles	0.35	93.0	7.0	
CALPHAD calculations at 1100 °C (Fig. 2)				
BCC1	0.67	61.4	38.6	
HCP	0.33	96.3	3.7	

from two phases, hexagonal close packed (HCP) and body centered cubic (BCC) (Fig. 1a). The HCP phase has the lattice parameters a = 318.1 pm and c = 504.2 pm and the BCC phase has the lattice parameter a = 335.6 pm. An SEM microstructure analysis shows that, in the HIP condition, the binary Hf-27Ta alloy has a coarse-grained structure, with the average grain size of ~ 1 mm (Fig. 1b). Higher magnification images, as well as EDS maps, indicate the presence of Hf-rich, rectangular-shaped large particles located both inside grains and at grain boundaries (Fig. 1c-f). The particles are \sim 3 µm wide and 10 µm long, in average, their volume fraction is ~35% and they consist of ~93%Hf and 7%Ta (Table 2). The continuous grain areas between the Hf-rich particles are rich in Ta (relative to the alloy composition, Fig. 1f, Table 2). Uneven contrast of these areas reveals lamellar-like structure, probably consisting of two phases (Fig. 1d), with the Ta-rich phase prevailing. Combining this information with the X-ray diffraction data, one can suggest that the Hf-rich phase has an HCP crystal structure and the Tarich phase is a BCC crystal structure.

Fig. 2a shows the equilibrium phase diagram for the Hf-Ta binary system [15] and Fig. 2b shows a calculated line projection of this diagram corresponding to 27 at.% Ta. (Pandat and ThermoCalc calculations showed the same results.) According to these phase diagrams, Ta has unlimited solubility in BCC Hf at high temperatures below the solidus. At lower temperatures, the Hf-Ta alloys with the amounts of Ta less than 43% experience phase transformation during which the hightemperature BCC1 phase partially transforms to a primary Hf-rich HCP phase. At even lower temperature of 1084 °C, the BCC1 phase experiences a monotectoid transformation with the formation of a secondary Hf-rich HCP and a Ta-rich BCC2 (Fig. 2a). In the Hf-27Ta alloy, the high-temperature BCC1 phase solidifies at 2120 °C and the singlephase BCC1 region is present at temperatures down to 1178 °C (Fig. 2b). At lower temperatures, BCC1 completely transforms to the Tarich BCC2 and Hf-rich HCP. All BCC2 and $\sim 1/2$ (by volume) of HCP are the result of the monotectoid transformation and the other 1/2 of the HCP phase forms slightly above the monotectoid transformation temperature (at 1084-1178 °C) (Fig. 2b).

This analysis indicates that the Hf-27%Ta alloy had a single-phase BCC crystal structure when it was HIP'd at 1400 °C and the observed microstructure was formed during the following cooling process. Comparison of the experimentally observed microstructure and phases in Hf-27Ta (Fig. 1) with the equilibrium phase diagrams (Fig. 2) suggests that the large Hf-rich particles formed above the monotectoid transformation temperature and the Ta-rich areas between these particles experienced the monotectoid transformation with the formation of two lamellar phases, BCC2 and HCP. This suggestion is also supported by the fact that the measured composition and volume fraction of the Hf-rich particles are very similar to the calculated composition and volume fraction (=0.33) of the HCP phase at 1100 °C. The measured compositions of the remaining, Ta-rich two-phase (BCC2 + HCP) areas are very similar to the calculated composition of the BCC1 phase at 1100 °C, i.e. just above the monotectoid transformation temperature (Table 2).

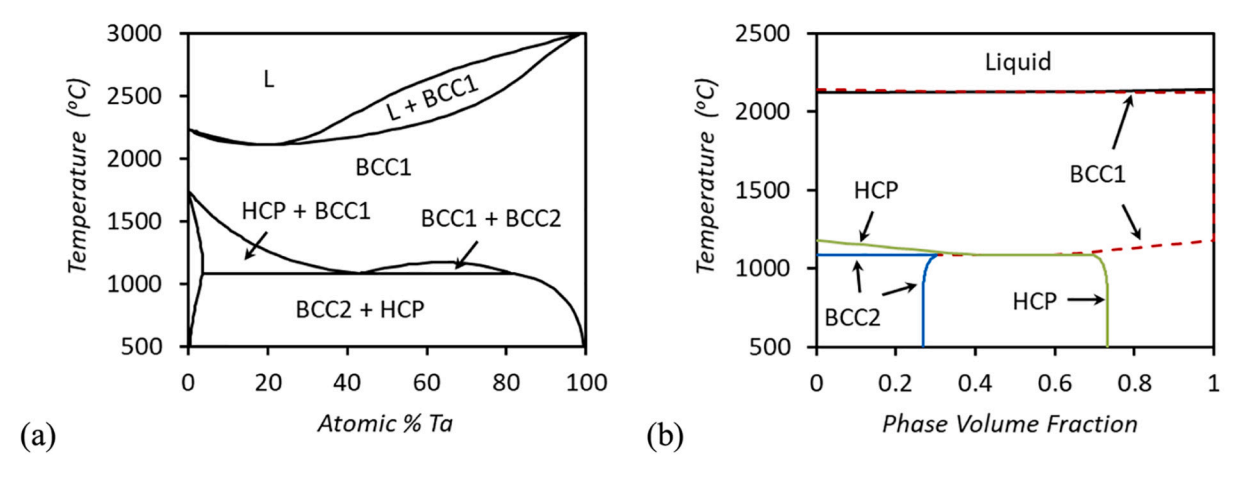


Fig. 2. (a) Equilibrium Hf-Ta binary phase diagram and (b) calculated equilibrium phases and their volume fractions in Hf-27%Ta in the temperature range of 500-2500 °C.

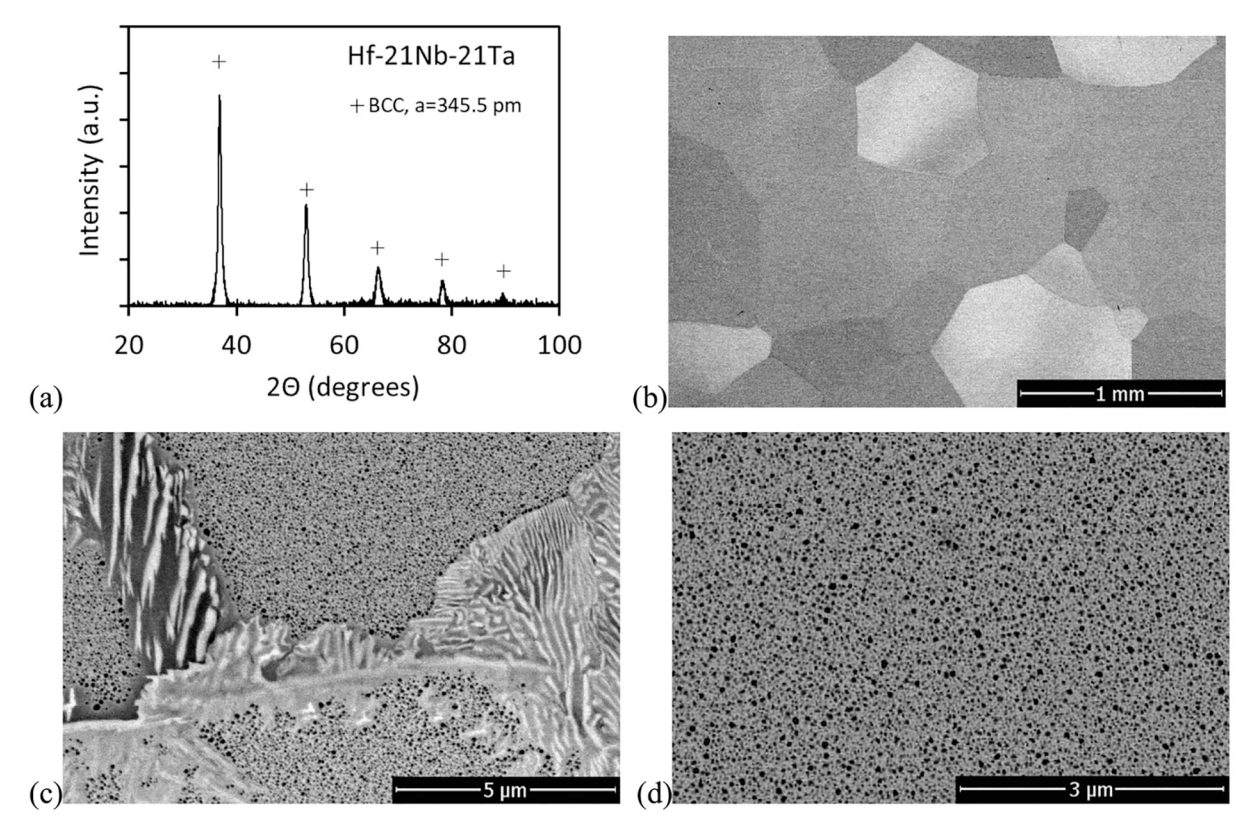


Fig. 3. (a) X-ray diffraction pattern and (b-d) BSE images of a HIP'd Hf-21Nb-21Ta alloy sample.

Table 3Chemical composition (in at.%) of different constituents in the Hf-21Nb-21Ta alloy, as determined by SEM/EDS.

Element	Hf	Nb	Ta
Intragranular (2-phase) region Bright phase	$60.0 \pm 0.3 \\ 68.6 \pm 1.0$	$20.5 \pm 1.8 \\ 15.4 \pm 0.8$	$19.5 \pm 0.5 \\ 16.0 \pm 0.8$
Dark Phase	56.4 ± 1.0	22.4 ± 1.0	21.2 ± 1.0

3.2. Microstructure of a Hf-21Nb-21Ta ternary alloy

An X-ray diffraction pattern from Hf-21Nb-21Ta contains diffraction peaks from a single BCC phase, which the lattice parameter is a =345.5

pm (Fig. 3a). The alloy has an equiaxed, polygonal grain structure, with the average grain size of $\sim\!0.4$ mm (Fig. 3b). Higher magnification backscatter electron (BSE) images reveal a eutectoid-like structure at grain boundaries (Fig. 3 c), which consists of at least two phases with different Z contrast and chemical composition (they are labeled as "Bright phase" and "Dark phase" in Table 3). The phase transformation likely started at grain boundaries and propagated inside grains producing bands consisting of two phases (Fig. 3c). The bright phase in these transformed regions is slightly rich in Hf and the dark phase is slightly rich in Nb and Ta relative to the average alloy composition (Table 3). Even higher magnification imaging reveals nanometer-sized spherical precipitates inside grains (Fig. 3d). These nano-precipitates have a dark contrast on the BSE images indicating smaller Z number relative to the matrix phase, which suggests that these precipitates are

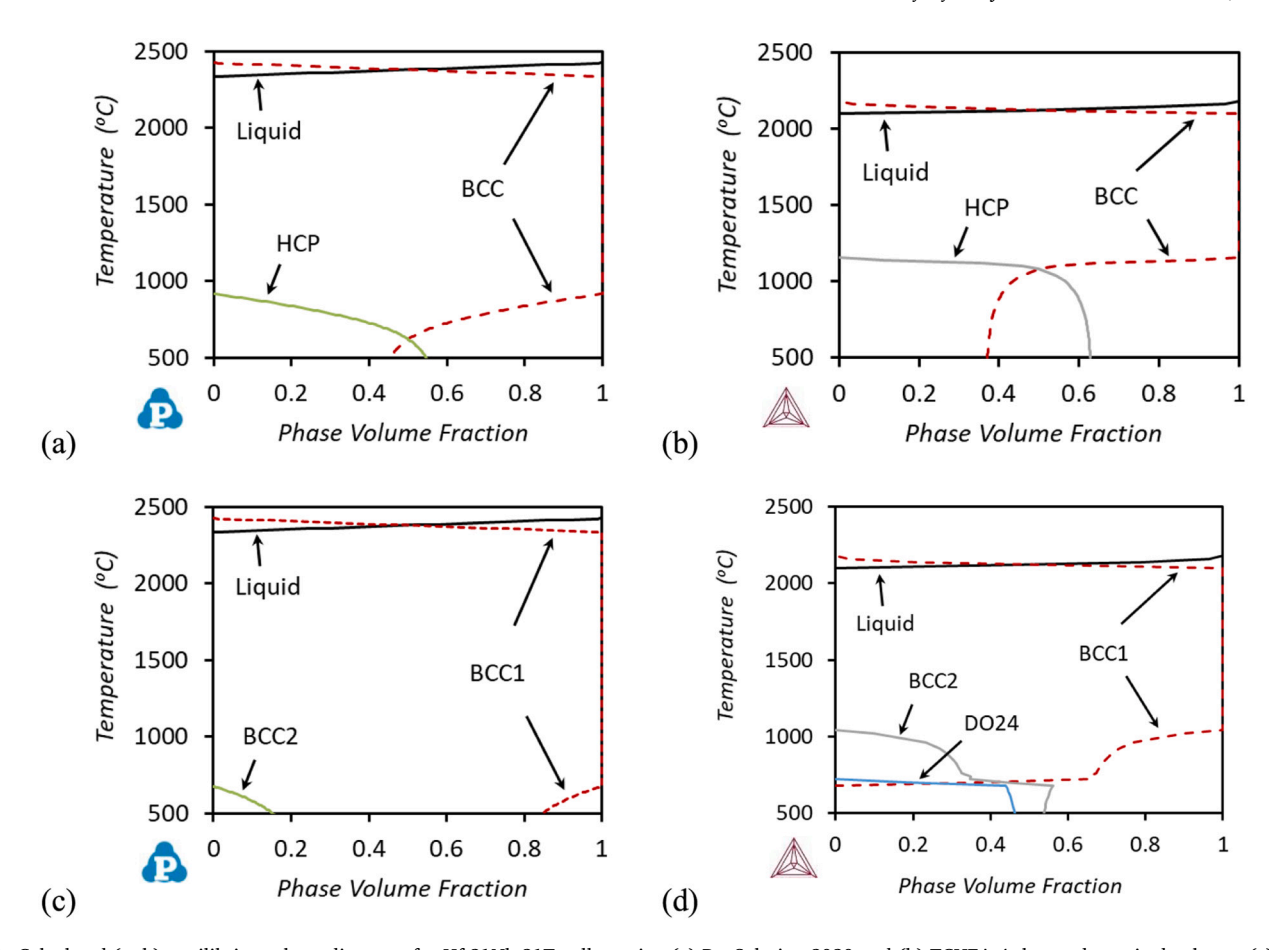


Fig. 4. Calculated (a, b) equilibrium phase diagrams for Hf-21Nb-21Ta alloy using (a) PanSolution-2020 and (b) TCHEA-4 thermodynamic databases. (c) A non-equilibrium phase diagrams calculated using (c) the PanSolution-2020 and (d) TCHEA-4 databases under suspension of hexagonal phases.

rich in Nb. Unfortunately, the composition of the nano-precipitates and the matrix phase cannot be measured separately by SEM/EDS due to the fine precipitate diameter and spacing, and the composition reported in Table 3 for intragranular regions is the average composition of these two phases. Additional TEM analysis is needed to reveal the composition and crystal structure of these precipitates.

Information on the thermodynamic properties of Hf-Nb-Ta ternary system is not available in the open literature. We have therefore calculated the equilibrium phase diagram for the Hf-21Nb-21Ta alloys using available thermodynamic properties of the respective binary systems and pure elements, using PanSolution-2020 and TCHEA-4 databases. The calculated diagrams are shown in Fig. 4a and Fig. 4b, respectively. They are qualitatively similar, as both the databases predict a hightemperature BCC region below the solidus and partial transformation of the BCC phase into Hf-rich HCP phase at lower temperatures. However, the phase transformation temperatures and volume fractions of the phases predicted by these two databases are different and both are in large disagreement with the experimental results. For example, according to PanSolution-2020 calculations, a high temperature singlephase BCC range is present at temperatures from 2334 °C (solidus) to 917 °C (HCP solvus), while according to TCHEA, this BCC range is present between 2107 °C and 1151 °C (Fig. 4 a, b). At lower temperatures, two phases, BCC and HCP, are present, with the volume fraction of HCP rapidly increasing toward ∼0.6 with decreasing the temperature down to 500 °C. However, no HCP phase was identified by X-ray diffraction (Fig. 3a). It was neither identified using SEM/EDS, as the HCP phase must be heavily enriched (>90%) with Hf, while the maximum amount of Hf in the alloy constituents do not exceed 70% (Table 3). Nevertheless, secondary BCC phase precipitation inside grains and two-phase lamellar regions at grain boundaries are clearly identified in this alloy. It is quite possible that the experimentally observed phases are metastable and are the result of slow diffusion kinetics of the alloying elements during cooling after HIP at 1400 °C. Formation of the HCP phase, highly enriched in Hf, requires diffusion of almost all Nb and Ta out of this phase, which can be kinetically restricted at temperatures below 917 °C. This suggestion is supported by a recent report on amorphization in the Hf-Nb-Ta system at near-equiatomic concentrations of the alloying elements [16]. The experimental observations suggest that a secondary BCC phase, instead of the calculated HCP, forms at T < 1400 °C in Hf-21Nb-21Ta. In our additional calculations we thus suppressed the formation of a hexagonal phase, and these calculations then predicted formation of a second BCC phase, but at even lower temperature (e.g. solvus at 674 °C in accord to PanSolution or 1020 °C in accord to TCHEA) than the calculated solvus for HCP (Fig. 4 c, d). This may explain heterogeneous nucleation of the second phase at grain boundaries, very small differences in the compositions of the two neighboring phases from the average alloy composition, and formation of very fine nano-precipitates inside grains. It is likely that these two BCC phases have very similar lattice parameters and are recognized on the XRD pattern as a single BCC phase. Additional microstructural examination after prolonged annealing at different temperatures is required to identify equilibrium phases in this alloy. The thermodynamic parameters related to the Hf-Nb-Ta ternary system need to be refined in both of the CALPHAD databases used in this work.

3.3. Microstructure of a Hf-21Mo-21Ta ternary alloy

According to X-ray diffraction, two phases, BCC and HCP, are present in the Hf-21Mo-21Ta alloy (Fig. 5a). Intensities of the diffraction peaks from the BCC phase are much higher than from the HCP phase, which

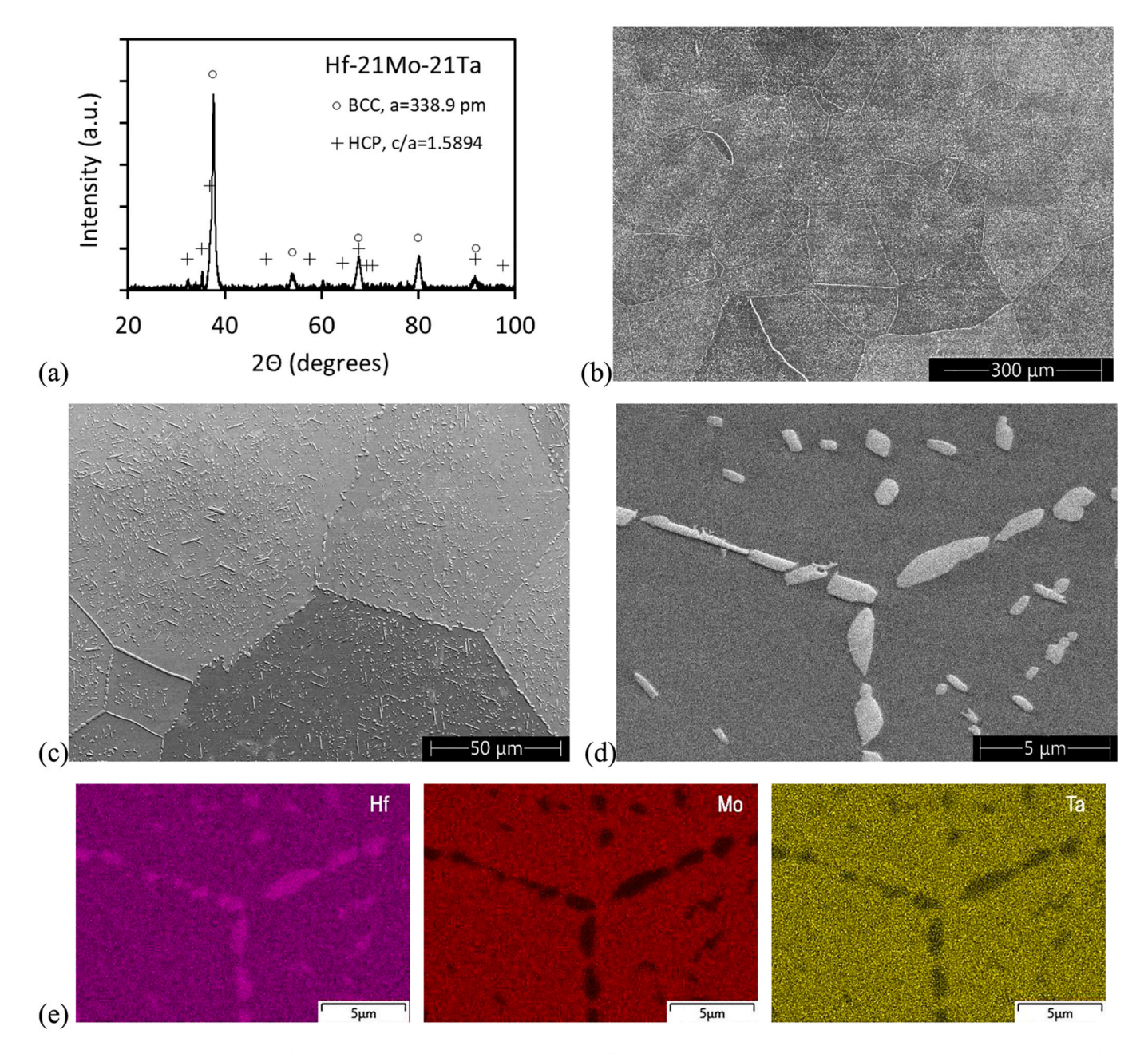


Fig. 5. (a) X-ray diffraction pattern and (b-d) SEM images of a HIP'd Hf-21Mo-21Ta alloy sample. (e) Elemental maps showing that the precipitates in figure (d) are rich in Hf and depleted in Mo and Ta.

Table 4Chemical composition (in at. %) of different constituents in the Hf-21Mo-21Ta alloy, as determined by SEM/EDS.

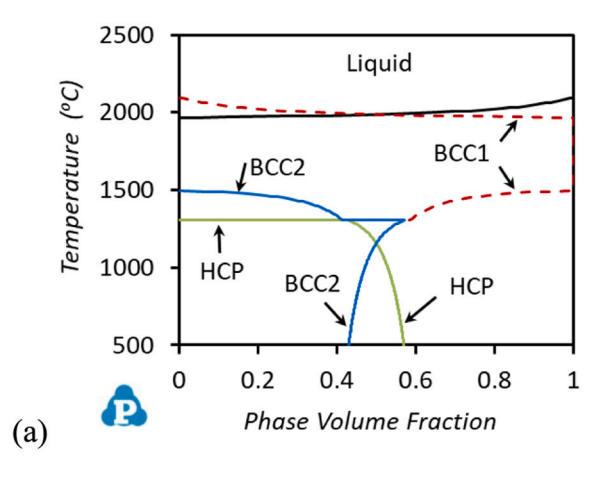
Element	Hf	Mo	Ta
Alloy (Fig. 5 b) Matrix Phase Particles	$60.5\\56.3 \pm 0.9\\94.8 \pm 2.8$	$19.1\\22.2\pm0.8\\2.0\pm1.3$	$\begin{array}{c} 20.4 \\ 21.5 \pm 0.4 \\ 3.2 \pm 1.7 \end{array}$

indicates that BCC is the major phase in the alloy. The lattice parameter of the BCC phase is a=339.8 pm. The HCP phase has the lattice parameters a=319.7 pm and c=508.2 pm, so that the ratio c/a=1.5894.

SEM shows that Hf-21Mo-21Ta has an equiaxed grain structure with the average size of 145 μm (Fig. 5b). Higher magnification images reveal the presence of a secondary phase, which precipitates at grain boundaries and inside grains (Fig. 5 c, d). The SEM/EDS analysis shows that

the second-phase particles are rich in Hf (Fig. 5e, Table 4). The matrix phase has a composition, which is only slightly different from the composition of the alloy (Table 4). Combining this information with the results from X-ray diffraction, one may conclude that the addition of Mo to Hf-27Ta stabilizes the BCC phase, which is present in Hf-21Mo-21Ta at room temperature in the form of the matrix phase. The volume fraction of secondary, Hf-rich precipitates is $\sim\!10\text{--}15\%$, and they are likely the HCP phase.

The calculated equilibrium phase diagram of the Hf-21Mo-21Ta alloy using PanSolution-2020 or TCHEA-4 thermodynamic databases are shown in Fig. 6a and Fig. 6b, respectively. According to PanSolution-2020, the alloy solidifies at 1966 $^{\circ}\text{C}$ and the single BCC1 phase region is present at temperatures down to 1496 $^{\circ}\text{C}$. At lower temperatures, the high-temperature BCC1 phase partially transforms to a BCC2 phase, which has a near-equimolar composition, the volume fraction of the BCC1 phase decreases with decreasing temperature and it becomes rich



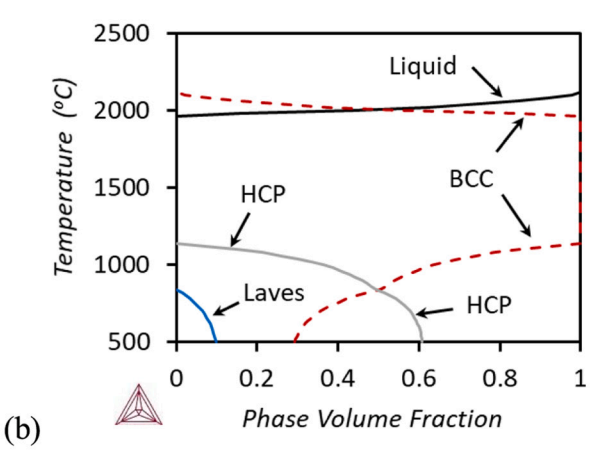


Fig. 6. Calculated equilibrium phase diagrams (phase volume fraction vs. temperature) of the Hf-21Mo-21Ta alloy using (a) PanSolution-2020 database or (b) TCHEA-4 database.

Table 5 Volume fraction (V_f) and composition (in at.%) of different phases predicted in Hf-21Mo-21Ta at 1400 °C and 1100 °C using CALPHAD approach and available thermodynamic database.

T (°C)	Phase	$V_{\rm f}$	Hf	Mo	Ta
PanSolution	n-2020				
1400	BCC1	0.654	71.3	14.6	14.1
1400	BCC2	0.346	32.9	33.1	33.9
1100	BCC2	0.487	14.8	42.8	42.4
1100	HCP	0.513	99.0	0.4	0.6
TCHEA-4					
1400	BCC	1.00	58.0	21.0	21.0
1100	BCC	0.85	51.7	24.2	24.1
1100	HCP	0.15	97.9	0.8	1.3

in Hf (Fig. 6a; Table 5, 1400 °C). The volume fraction of the BCC1 phase at 1400 °C is 0.654. At 1305 °C a monotectoid phase transformation is predicted in this alloy, during which the Hf-rich BCC1 phase transforms to a Hf-rich HCP phase and Mo and Ta rich BCC2 phase (Fig. 6a). At 1100 °C, the volume fractions of the BCC2 and HCP phases are predicted to be 0.49 and 0.51, respectively (Table 5). This calculated phase diagram strongly disagrees with the experimental results, which show no evidence of the monotectoid phase transformation and a considerably lower volume fraction of the HCP phase. Thermodynamic parameters for the Hf-Mo-Ta system in PanSolution-2020 database require refinement.

The phase diagram calculated using TCHEA-4 database (Fig. 6b) agrees better with the experimental data. According to these calculations, the high-temperature BCC phase partially transforms to a Hf-rich HCP phase at temperatures below 1120 °C and additionally to a Laves (HfMo₂) phase below 820 °C. The calculations predict about 60% of HCP and 10% of Laves at equilibrium at 500 °C (Fig. 6b). The much lower volume fraction of the HCP phase and the absence of the Laves phase observed in Hf-21Mo-21Ta can be explained by insufficient diffusion kinetics of the alloying elements at temperatures below 1120 °C during cooling from 1400 °C. According to TCHEA-4 calculations, 15% by volume fraction of the HCP phase in equilibrium corresponds to T =1100 °C, where the HCP phase consists of 97.9% Hf, 1.3%Ta and 0.8% Mo and the BCC phase consists of ~51.7%Hf, 24.1%Ta and 24.2%Mo (Table 5). These calculated compositions of the BCC and HCP phases are close to the respective compositions determined experimentally (Table 4). One can therefore suggest that the microstructure of the Hf-21Mo-21Ta observed at room temperature was quenched from \sim 1100 °C.

3.4. Microstructure of a Hf-21Ta-21W ternary alloy

The X-ray diffraction pattern from Hf-21Ta-21W contains diffraction peaks from at least three phases (Fig. 7a). In particular, diffraction peaks from an HCP phase, a cubic Laves phase and a BCC phase are identified. According to the intensity of the diffraction peaks, the HCP and Laves are major phases and BCC is the minor phase. The lattice parameters of the HCP phase are $a=319.0\,$ pm and $c=505.9\,$ pm. The lattice parameter of the cubic Laves (C15) phase is 765.6 pm and the lattice parameter of the BCC phase is $a=334.8\,$ pm (Fig. 7a).

The microstructure of Hf-21Ta-21W consists of equiaxed grains, with the average grain size of \sim 75 μm (Fig. 7 b). High volume fractions of secondary phases are present in the form of micrometer-sized equiaxed and elongated particles and nanometer-sized lamellae (Fig. 7 c-e). The second-phase particles are present both at grain boundaries and inside grains, and grain boundary particles are almost twice as large (Fig. 7c). SEM/EDS analysis identifies three characteristic constituents in the microstructure. These are (a) Hf-rich regions, inside grains, which volume fraction is ~40%, (b) large, W-rich second phase particles, both inside grains and at grain boundaries, which volume fraction is $\sim 30\%$, and (c) two-phase lamellar regions, inside grains, which are rich in Ta and Hf and depleted with W and which volume fraction is estimated to be \sim 30% (Fig. 7 d-f, Table 6). Comparing the SEM/EDS data with the Xray diffraction results one can suggest that the Hf-rich regions likely have the HCP crystal structure, and the W-rich regions represent a cubic (C15) Laves phase. The morphology of the Ta- and Hf- rich lamellae regions suggests that these regions experienced a monotectoid transformation and likely consist of a Ta-rich BCC phase and a Hf-rich HCP phase.

The equilibrium phase diagrams of Hf-21Ta-21W calculated using PanSolution-2020 or TCHEA-4 Calphad databases are shown in Fig. 8a and Fig. 8b, respectively. According to PanSolution-2020, after solidification at 1978 °C, the Hf-21Ta-21W alloy consists of two BCC phases: BCC1 is rich in Ta and W and BCC2 is rich in Hf. (Fig. 8a). Upon cooling in the temperature range from 1403 °C to 1378 °C the BCC2 phase partially (\sim 11%) transforms to a Hf-rich HCP phase and at 1338 °C the remaining BCC2 phase experiences a monotectoid transformation to a Hf-rich hexagonal phase and a Ta and W rich BCC1 phase. The calculated phase volume fractions and phase compositions at 1400 °C (three-phase region) and at 1100 °C (two-phase region below the monotectoid transformation) are given in Table 7. At temperatures below 753 °C the disordered BCC1 phase transforms into an ordered B2. Two phases, Ta and W rich B2 and Hf-rich HCP, are present in equilibrium at 500 °C (Table 7).

The phase diagram calculated using TCEA-4 database is noticeably different (Fig. 8b). This diagram predicts a single-phase BCC region

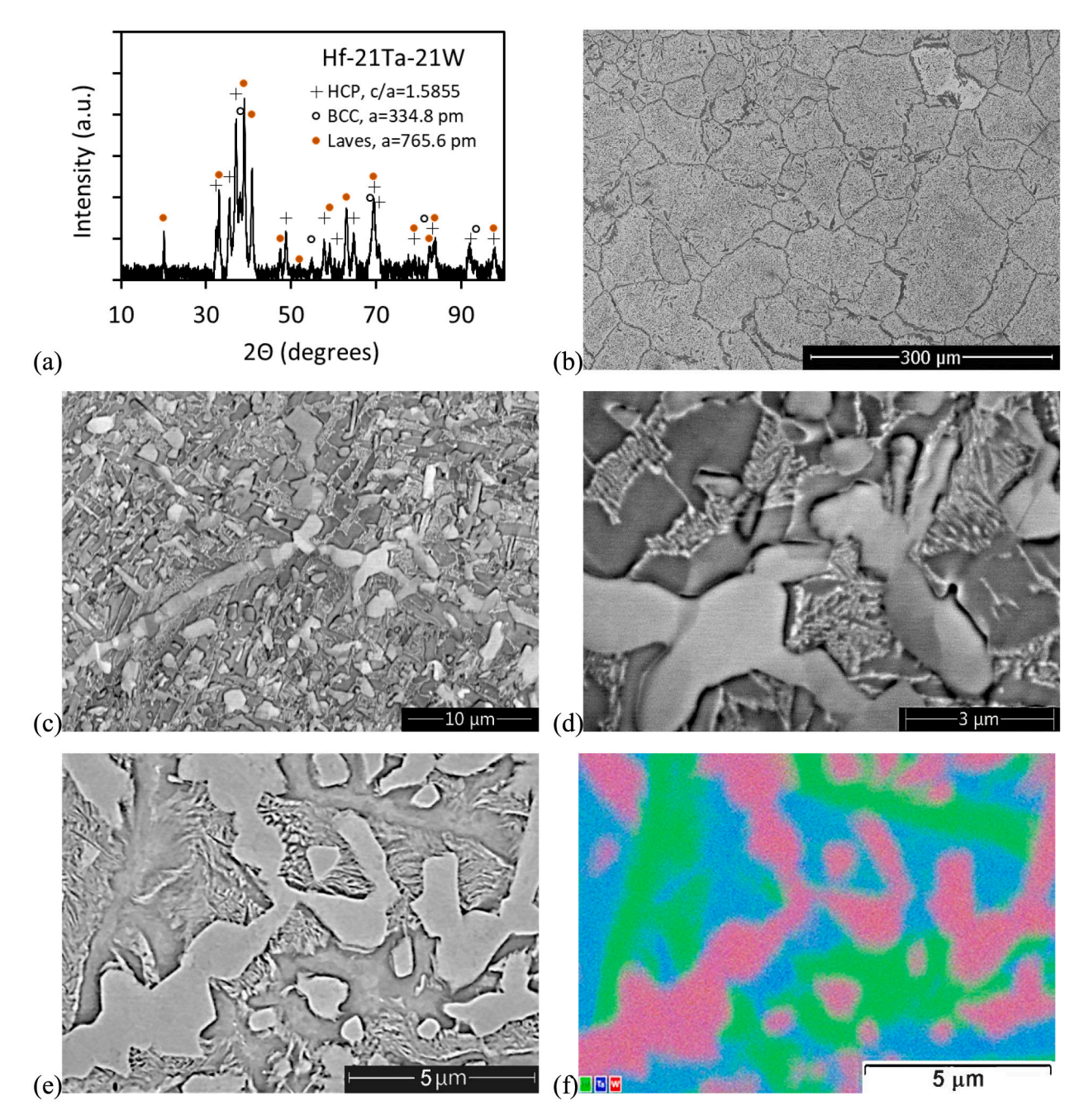


Fig. 7. (a) X-ray diffraction pattern, (b) secondary electron image and (c-e) backscatter electron images of a HIP'd Hf-21Ta-21W alloy sample. (f) Composition map showing preferential distribution of the alloying elements (green is Hf, blue is Ta and red is W) in the sample area shown in figure (e). (For interpretation of the references to color in this figure legend, the reader is referred to the web version of this article.)

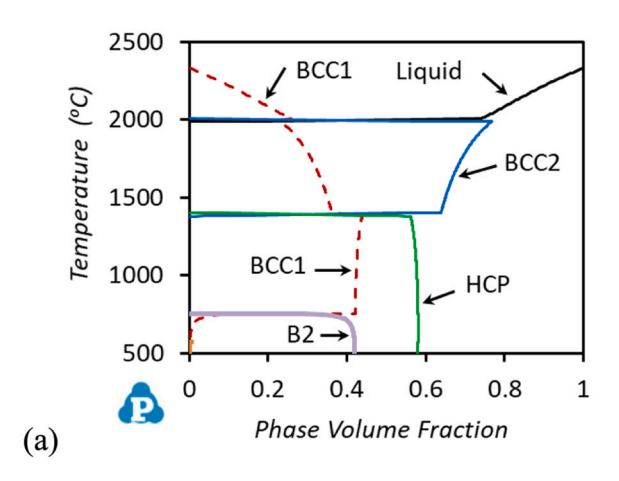
 $\label{eq:table 6} Table 6 \\ Volume fraction (V_f) and chemical composition (in at.%) of different constituents in the Hf-21Ta-21W alloy, as determined by SEM/EDS (Fig. 7).$

Element	V_{f}	Hf	Ta	W
Whole area (Fig. 7b)	1	60.2	20.7	19.1
Hf-rich regions	0.40	90.1 ± 2.2	7.3 ± 1.5	2.6 ± 1.0
W-rich regions	0.30	36.0 ± 0.9	22.1 ± 0.4	$\textbf{41.9} \pm \textbf{1.2}$
Ta-rich lamella (2-phase)	0.30	64.9 ± 3.4	30.3 ± 2.9	4.8 ± 1.2
regions				

below the solidus (\sim 2000 °C). The BCC phase partially transforms to a cubic Laves phase (HfW₂) at temperatures below 1680 °C. At T=1400 °C, TCHEA-4 predicts the presence of two phases, BCC and Laves,

at the volume fractions of 0.89 and 0.11, respectively (Table 7). A monotectoid transformation of the high-temperature BCC phase to the Ta-rich BCC2 and Hf-rich HCP is predicted to occur at 1180 °C. At T=1100 °C, i.e. almost immediately after the transformation, the volume fractions of the Laves, BCC2 and HCP phases are 0.16, 0.27 and 0.57, respectively, and these proportions retain down to 500 °C (Fig. 8b). It should be noted that TCHEA-4 predicts high volume fraction (\sim 0.84) of the monotectoidally transformed regions. The HCP phase is predicted to reside inside these regions only.

Comparison of the calculated phase diagrams with the experimental results indicates that PanSolution-2020 fails to predict formation of the Laves phase, which measured volume fraction is rather large (\sim 30%), and TCHEA-4 fails to predict the presence of a primary HCP phase at temperatures above the monotectoid reaction, which measured volume



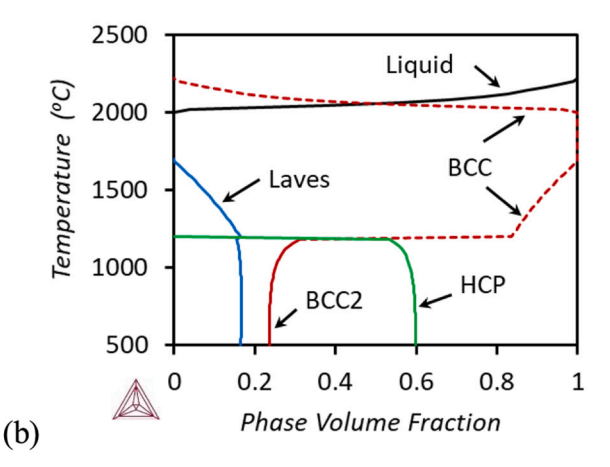


Fig. 8. Equilibrium phase diagrams for Hf-21Ta-21W alloy calculated using (a) PanSolution-2020 database and (b) TCHEA-4 database.

Table 7 Volume fraction and composition (in at.%) of different phases predicted in Hf-21Ta-21W at 1900 $^{\circ}\text{C}$, 1400 $^{\circ}\text{C}$ and 1100 $^{\circ}\text{C}$ using CALPHAD approach and available thermodynamic database.

T (°C)	Phase	Vf	Hf	Ta	W
PanSolution-	2020				
1400 °C	BCC1	0.36	6.7	42.8	50.5
1400 °C	BCC2	0.54	86.9	9.2	3.9
1400 °C	HCP	0.10	98.0	1.7	0.30
1100 °C	BCC1	0.42	2.8	47.9	49.3
1100 °C	HCP	0.58	98.8	1.1	0.1
TCHEA-4					
1400	BCC	0.89	63.0	13.5	23.5
1400	Laves	0.11	34.1	57.1	8.8
1100	Laves	0.16	33.7	10.1	56.2
1100	BCC2	0.27	12.2	63.2	24.6
1100	HCP	0.57	97.7	2.2	0.1

fraction is ~40%. Both databases predict correctly that the Hf-rich HCP phase is one of the major phases in the alloy and that the alloy experiences a monotectoid phase transformation. These transformed regions are recognized as two-phase lamellar areas on the BSE images (Fig. 7 d, e). The morphology of the phases experimentally observed in the Hf-21Ta-21W alloy indicates that only \sim 30% of the alloy experiences a monotectoid phase transformation, while PanSolution-2020 predicts ~55% and TCHEA-4 predicts 84% of the alloy to experience this transformation (Fig. 8). This discrepancy cannot be explained by slow diffusion kinetics of Ta and W, as the incomplete monotectoid transformation should result in a relatively large volume fraction of a residual, Hf-rich BCC phase. However, this phase was not detected by X-ray diffraction and SEM/EDS. Only a Ta-rich BCC phase inside the monotectoid lamellar domains was present. The morphology of the grain structure suggests that during annealing at 1400 °C the alloy was a predominantly single-phase structure rather than a two-phase duplex structure.

Table 8 Vickers microhardness (Hv), yield stress (σ_y) , true peak stress (σ_p) and respective true peak strain (ϵ_p) , and true fracture strain (ϵ_f) of the studied alloys at room

<i>T</i> = 25 °C	$\mathrm{Hf_{73}Ta_{27}}$	$Hf_{58}Mo_{21}Ta_{21}$	$\mathrm{Hf_{58}Nb_{21}Ta_{21}}$	$Hf_{58}Ta_{21}W_{21}$
Hv	490	513	289	522
σ _v (MPa)	1708	1496	832	1475
σ _p (MPa)	1940	1580	1204	1883
ϵ_{p}	0.106	0.031	0.554	0.059
$\epsilon_{ m f}$	0.129	0.048	0.559	0.067

Based on the above discussion, one can suggest the following phase transformations in the Hf-21Ta-21W alloy. The alloy solidifies in a single-phase BCC structure, which upon cooling partially transforms to a Laves and HCP phases before the monotectoid transformation occurs at lower temperatures. At 1400 $^{\circ}\text{C}$, the alloy still retains the BCC matrix phase as the major phase, although small amounts of the Laves and HCP phases may already be present. At the temperature slightly above the temperature of monotectoid transformation, the alloy contains three phases, W-rich Laves, Hf-rich HCP and remaining Hf + Ta-rich BCC, at the volume fractions of $\sim\!0.3$, 0.4 and 0.3. During the monotectoid transformation, the remaining BCC transforms to a Ta-rich BCC2 and Hf-rich secondary HCP phase. It appears that both databases should be refined to predict such set of phase transformations in the Hf-Ta-W system.

Despite the apparent similarity of the four systems, the interpreted phase evolution of each varies in character (Fig. 9), though there is significant uncertainty due to the limited fidelity of the CALPHAD databases. As expected from the binaries, Mo and W additions lead to the formation of Laves phases and the formation of an HCP phase. The addition of Nb to Hf-27Ta suppresses the HCP phase, as expected from the binaries, by the reduction of Hf and its extensive solubility in Nb and Ta. In all cases, there are second (or third) phases that could be expected to provide a strength benefit (HCP and Laves especially), but they are unstable as the temperature rises toward 1400 $^{\circ}\text{C}.$

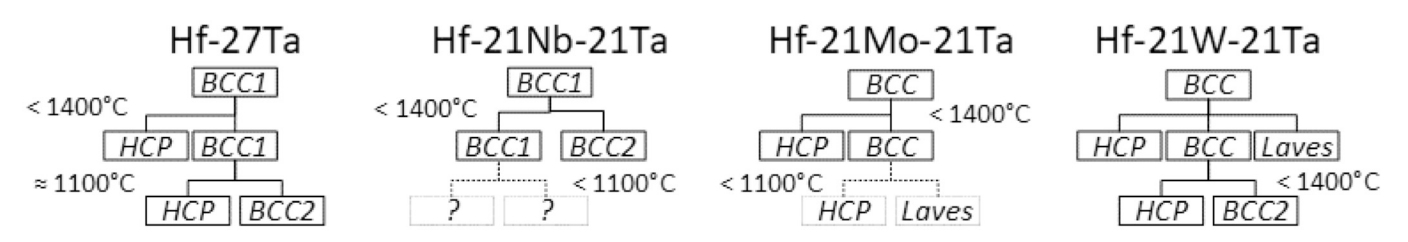


Fig. 9. Summary of observed (solid boxes and connecting lines) and expected (dashed boxes and connecting lines) phases and reactions. In each case the primary solidification phase is BCC follows by a series of decomposition reactions.

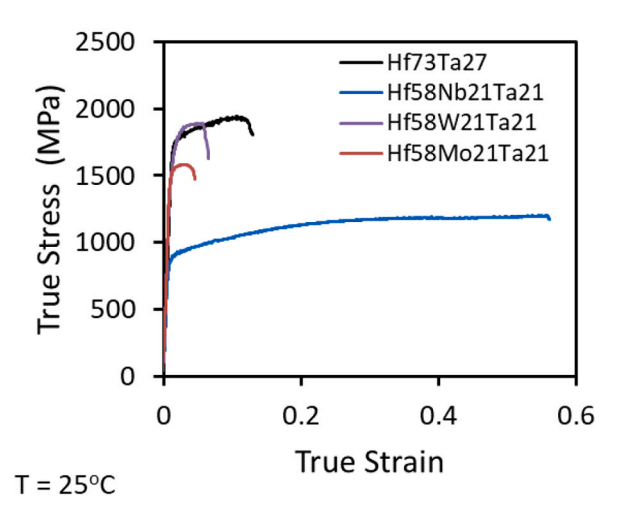


Fig. 10. Room temperature true stress versus true strain compression curves of the studied alloys.

3.5. Mechanical properties

The binary Hf-27Ta alloy has room temperature Vickers microhardness Hv = 490 \pm 8. The microhardness decreases considerably, to Hv = 289 \pm 7, in ternary Hf-21Nb-21Ta. The ternary alloys with Mo (Hf-21Mo-21Ta) and with W (Hf-21Ta-21W) have slightly increased

microhardness values, Hv = 513 ± 10 and Hv = 522 ± 5 , respectively, relative to the binary alloy (Table 8). It is concluded that the Nb addition softens while Mo or W additions harden the Hf-27Ta alloy.

Fig. 10 illustrates room temperature true stress versus true strain deformation curves and Table 8 shows room temperature mechanical properties of the studied alloys. The binary alloy has the yield stress σ_v = 1708 MPa, its true stress increases with increasing strain and reaches the peak value, $\sigma_p = 1940$ MPa at $\epsilon_p = 0.106$. Fracture of Hf-Ta occurs shortly after reaching the peak stress, at true strain $\epsilon_f=0.129.$ The ternary alloys have smaller yield stress values, 1496 MPa, 1475 MPa and 832 MPa for Hf-Mo-Ta, Hf-Ta-W and Hf-Nb-Ta, respectively. The ternary alloys with Mo and W also have reduced compression fracture strain, ε_f = 0.048 and 0.067, respectively. A slightly higher true fracture strain of Hf-Ta-W, than that of Hf-Mo-Ta, is likely due to stronger strain hardening, which also results in a larger peak stress and fracture stress in Hf-Ta-W (Fig. 10, Table 8). The Hf-Nb-Ta alloy has the lowest yield stress, but it is the most ductile ($\epsilon_f = 0.559$) among the studied alloys. The alloy shows moderate strain hardening, which results in achieving the true peak stress of $\sigma_p=$ 1204 MPa at $\epsilon_p=$ 0.554. The compression data indicate that not only additions of Nb, but also Mo or W decrease the room temperature strength of Hf-27Ta, which is somewhat different from the microhardness results. It looks like the surface layers of the Mo and W containing alloys are stronger than the bulk. The reasons are unclear.

The deformation behavior of the studied alloys at high temperatures ($\geq 1000\,^{\circ}\text{C}$) is illustrated in Fig. 11 and the high-temperature compression properties are given in Table 9. In this temperature

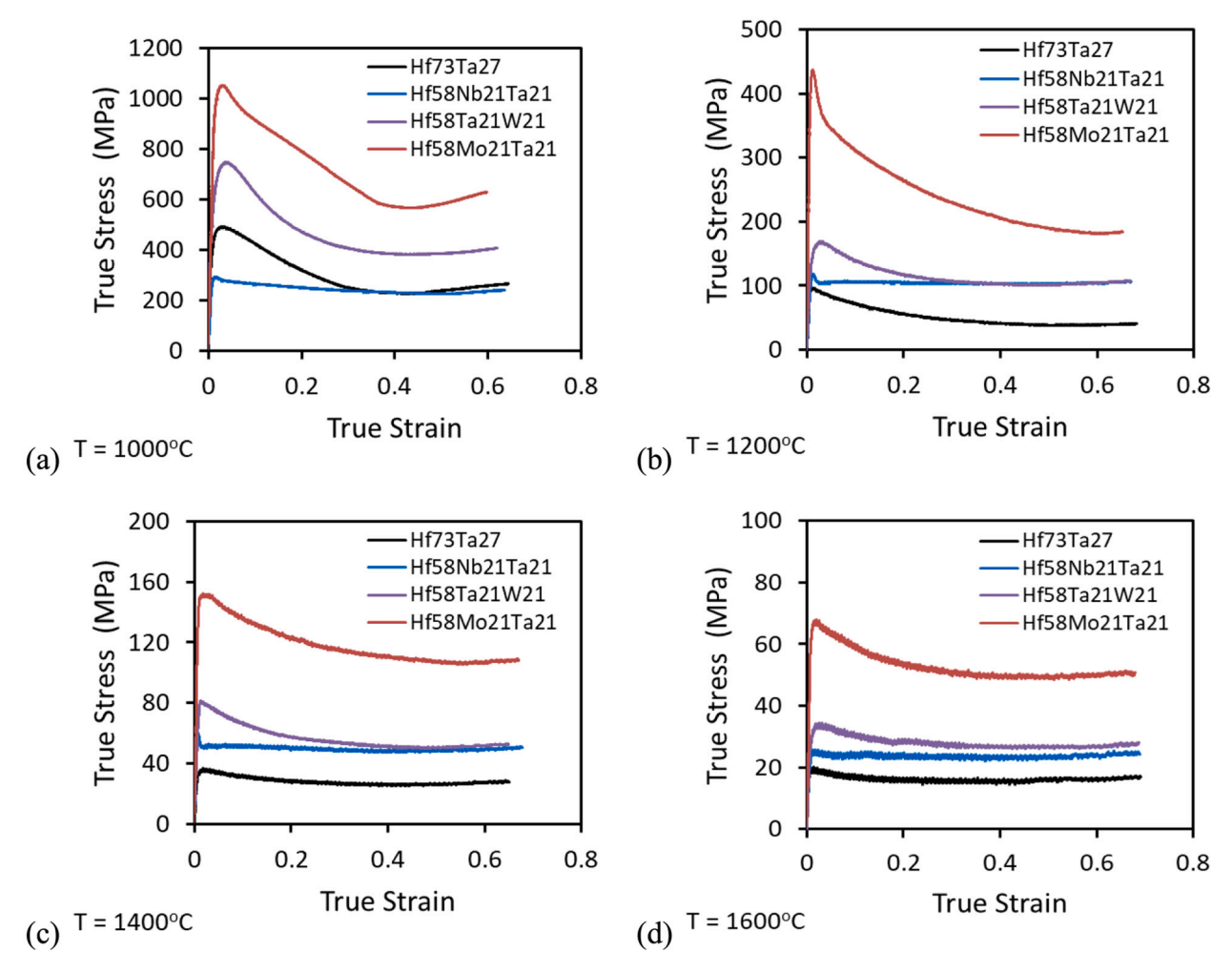


Fig. 11. True stress versus true strain deformation curves of the studied alloys at (a) $1000 \, ^{\circ}$ C, (b) $1200 \, ^{\circ}$ C, (c) $1400 \, ^{\circ}$ C and (d) $1600 \, ^{\circ}$ C.

Table 9 Yield stress (σ_y) , true peak stress (σ_p) and respective true peak strain (ϵ_p) , and true stress (σ_{20}) at true strain $\epsilon=0.2$ of the studied alloys at 1000 °C, 1200 °C, 1400 °C and 1600 °C.

	$Hf_{73}Ta_{27}$	$Hf_{58}Mo_{21}Ta_{21}$	$Hf_{58}Nb_{21}Ta_{21}$	$Hf_{58}Ta_{21}W_{21}$
T = 1000 °C				
σ _v (MPa)	353	943	278	480
σ _p (MPa)	492	1052	293	747
ε_{p}	0.028	0.030	0.016	0.039
σ ₂₀ , MPa	320	791	251	472
$T=1200~^{\circ}\mathrm{C}$				
σ _v (MPa)	94	421	118	137
σ _p (MPa)	97	437	118	169
ε_{p}	0.010	0.011	0.012	0.026
σ ₂₀ , MPa	56	263	104	117
1400 °C				
σ _y (MPa)	33	146	60	77
σ _p (MPa)	36	152	60	81
ε_{p}	0.018	0.017	0.007	0.014
σ_{20} , MPa	29	123	50	58
1600 °C				
σ _y (MPa)	18.8	64	23	28.3
σ _p (MPa)	20	68	26	35
ε_{p}	0.015	0.019	0.012	0.025
σ ₂₀ , MPa	16	53	24	28

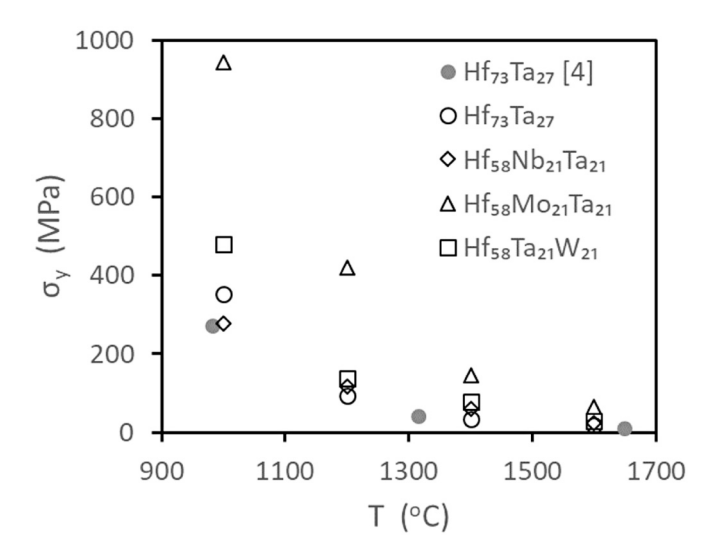


Fig. 12. Yield stress of studied alloys vs temperature. The compressive yield stress of the Hf-27Ta is compared to the tensile yield stress of the same alloy reported by Marnoch [4].

range, the alloys show a brief strain hardening stage at the beginning of deformation and the maximum (peak) stress is achieved at true strains $\epsilon_p \leq 0.03$. After that, strain softening, which can follow by steady state flow, occurs. The stress increases observed at true strains above \sim 0.4 are likely due to developing friction stresses between the die and sample surfaces; however, no noticeable barreling of the deformed samples was observed. All the alloys show good compression ductility and they did not fracture after 50% compression deformation (i.e. 0.693 true strain). Comparing the thermal softening of the alloys (Fig. 12), it is clear that the Hf-21Mo-21Ta alloy retains strength best among the studied alloys at high temperatures. At 1000 $^{\circ}C$ it has $\sigma_y = 943$ MPa and $\sigma_p = 1052$ MPa, retaining $\sim\!65\%$ of its room temperature strength, and shows a subsequent parabolic stress decrease with temperature approaching σ_v = 64 MPa and σ_p = 68 MPa at 1600 °C. The strength of the Hf-21Ta-21W is a distant second in this temperature range; its yield stress and peak stress at 1000 °C are lower by \sim 49% and 29% and at 1600 °C by 56% and 49%, respectively, than the same properties of Hf-21Mo-21Ta

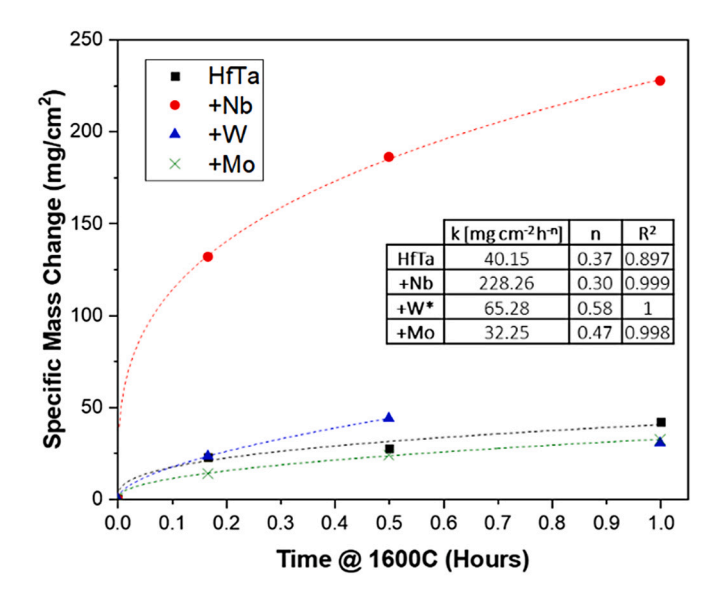


Fig. 13. Specific mass change plots of the studied alloys subjected to discontinuous oxidation in air at 1600 $^{\circ}$ C. Dotted curves represent exponential fitting (*60 min condition for Hf-Ta-W alloy is omitted); fitting parameters are shown in the inset table.

(Table 9). The Hf-21Nb-21Ta alloy is the weakest alloy at 1000 $^{\circ}$ C; however, the binary Hf-27Ta alloy becomes the weakest one at 1200 $^{\circ}$ C, 1400 $^{\circ}$ C and 1600 $^{\circ}$ C (Fig. 11, Table 9). The compressive yield stress of this binary alloy is similar to the tensile yield strength reported by Marnoch [4] (Fig. 12). The substitution of a more refractory element for Hf increases the strength of the ternary alloys at these three temperatures. However, not only does Mo impart more strength than the more refractory W, but based on the observed phase evolution (Fig. 9), one would expect that Hf-21Ta-21W would retain the most strength above 1400 $^{\circ}$ C due to the presence of both the Laves and HCP phases, which is not the case. Further studies are planned to understand why alloying with W has a weaker effect on the high-temperature strength than alloying with Mo.

3.6. Oxidation behavior

Comparative discontinuous oxidation studies were performed in an open-air box furnace. The specific mass gain calculated for each alloy after exposures at $1600\,^{\circ}\text{C}$ for 10, 30, and $60\,\text{min}$ is shown in Fig. 13. Qualitative EDS maps and corresponding BSE images of the oxide scales formed at the $10\,\text{min}$ condition are shown in Fig. $14\,\text{through}$ Fig. 17. The oxidation kinetics of each alloy system were fit to the general oxide growth rate law [17]:

$$\Delta m = kt^n \tag{1}$$

where Δm is the change in mass normalized to the initial surface area; k is the oxide growth rate constant; t is time in hours, and n is the time exponent (see inset table of Fig. 13). The Mo containing alloy exhibited near-parabolic oxidation kinetics (n=0.47), while the binary and Nb containing alloys displayed sub-parabolic regimes (n=0.37 and 0.30, respectively). The W-containing alloy exhibited two oxidation regimes: within the first 30 min, the specific mass of Hf-21Ta-21W increased and followed Eq. (1) with n=0.58; however, specific mass loss occurred at longer times (Fig. 13). It is likely that this delayed mass loss was caused by the selective evaporation of volatile W-oxides. This suggestion is also supported by the apparent concentration gradient of W in the oxide scale seen in the EDS element maps (Fig. 17).

Microstructural and chemical analyses of the oxide scales formed at $1600\,^{\circ}$ Cshowed a Ta-rich oxide layer of varying thicknesses at the oxide surface of all the studied alloys except Hf-21Nb-21Ta (see Fig. 14

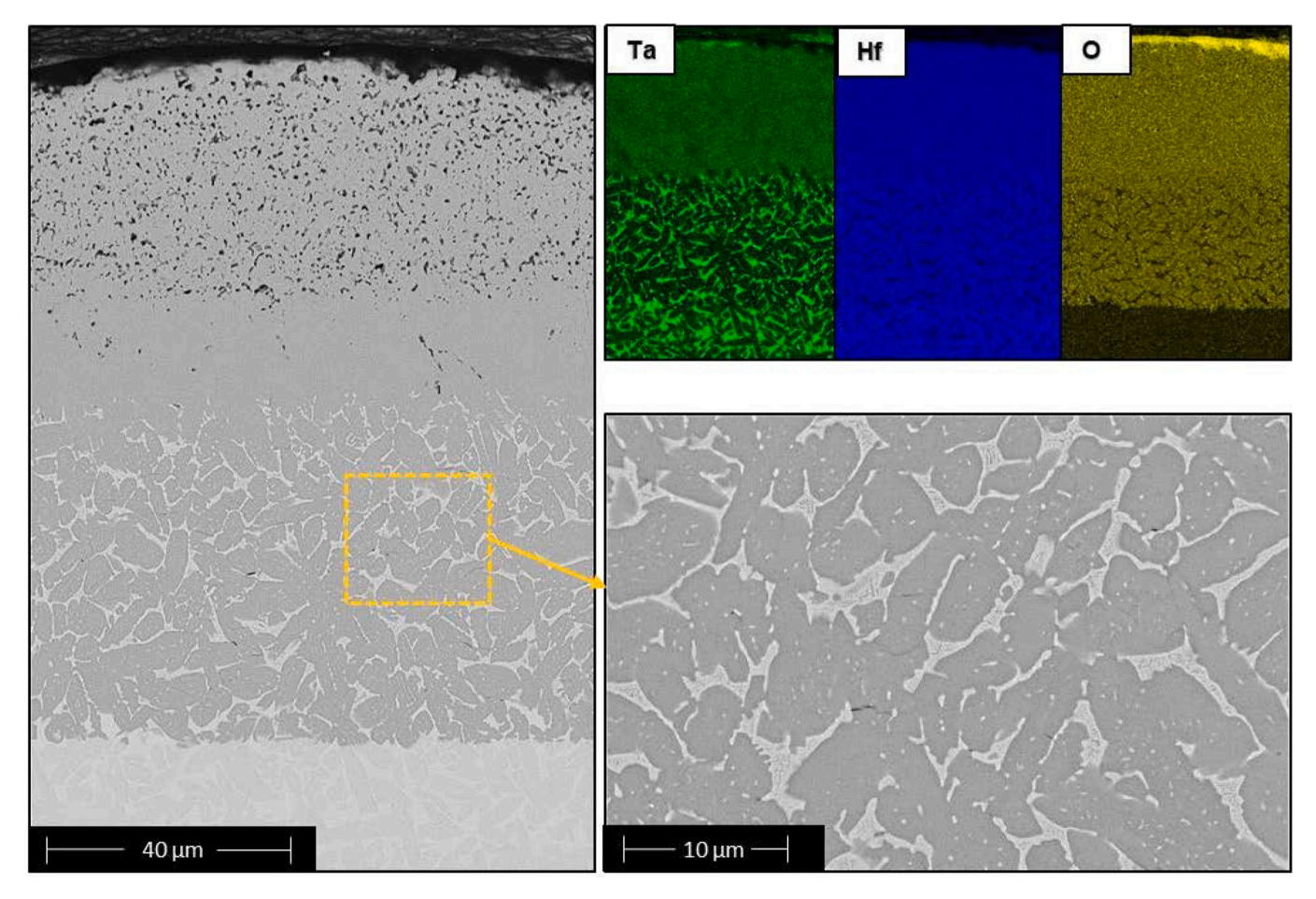


Fig. 14. BSE micrographs and EDS element maps of oxide scale formed on the Hf-27Ta binary alloy after oxidation at 1600 °C for 10 min in air.

through Fig. 17). All the alloys exhibited porous scales of different morphologies and indications of multi-front internal oxidation. While the Hf-27Ta (Fig. 14) and Hf-21Mo-21Ta (Fig. 15) alloys displayed a compact porosity network, the Hf-21Nb-21Ta (Fig. 16) and Hf-21Ta-21W (Fig. 17) alloys appeared to form "trails" of pores directed toward the scale surface. The latter observation likely indicates counterdiffusion of gaseous and/or liquid species emanating outward to the surface, due to the high volatility of W-oxides (e.g. WO₃) and potentially low melting points of common Nb-oxides (e.g. Nb₂O₅). A considerably reduced amount of Mo in the oxide scale formed on the Hf-21Mo-21Ta alloy can also be explained by the volatility of Mo-oxides (e.g. MoO₃) [18]. The oxide scale of all the alloys, except Hf-21Mo-21Ta, was predominantly adherent, however, cracking was observed near porosity channels, at oxide-consumed grain boundaries, and at the oxide-bulk interface. In the case of Hf-21Mo-21Ta, the oxide cracking was the most severe: although the surface scale did not entirely spall upon cooling, the oxide-bulk bond was the weakest for this alloy, thus requiring "re-attachment" of the oxide to the bulk for the microstructural evaluation. Although a great care was taken to handle the oxide layers (including epoxy encapsulation) during metallographic preparation, there is a possibility that some cracks formed and/or original crack propagated during the sample preparation due to oxide brittleness. Therefore, at the present time we cannot confirm whether the observed cracks formed during oxidation, upon cooling due to disparate coefficients of thermal expansion [19], or during sample preparation.

Post-oxidation XRD analysis of the binary Hf-27Ta alloy (Fig. 18) revealed a strong presence of the HfTaO superstructure (e.g. $\rm Hf_6Ta_2O_{17}$) and a simple $\rm Ta_2O_5$ oxide, as described by McCormack and Kriven [20] and Yang et al. [6]. The diffraction peaks from these oxides were also observed as major peaks in all the oxidized ternary alloys, indicating preferred formation of these oxides in the studied alloys. Further interrogation of the internal oxide products for the ternary alloys is underway and a more complete structural description of the ternary oxide products will be reported in a future work.

4. Summary and conclusions

A binary Hf-27Ta alloy and three ternary alloys, Hf-21Mo-21Ta, Hf-21Nb-21Ta and Hf-21Ta-21W (compositions are in at. %) were produced by vacuum arc melting. To reduce casting defects, the alloys were hot isostatically pressed by holding for 3 h at 1400 °C under a pressure of 207 MPa in high-purity argon and then slow cooled to room temperature. Microstructure, mechanical properties (at 25 °C, 1000 °C, 1200 °C, 1400 °C and 1600 °C) and oxidation behavior (at 1600 °C) of the alloys were studied. The observed phase compositions were compared with Calphad calculated phase diagrams for the respective alloys to validate currently available Calphad databases, PanSolution-2020 and TCHEA-4. Below the main results are briefly outlined.

The microstructure of the binary Hf-27Ta alloy consisted of coarse primary HCP particles and a monotectoidally transformed matrix

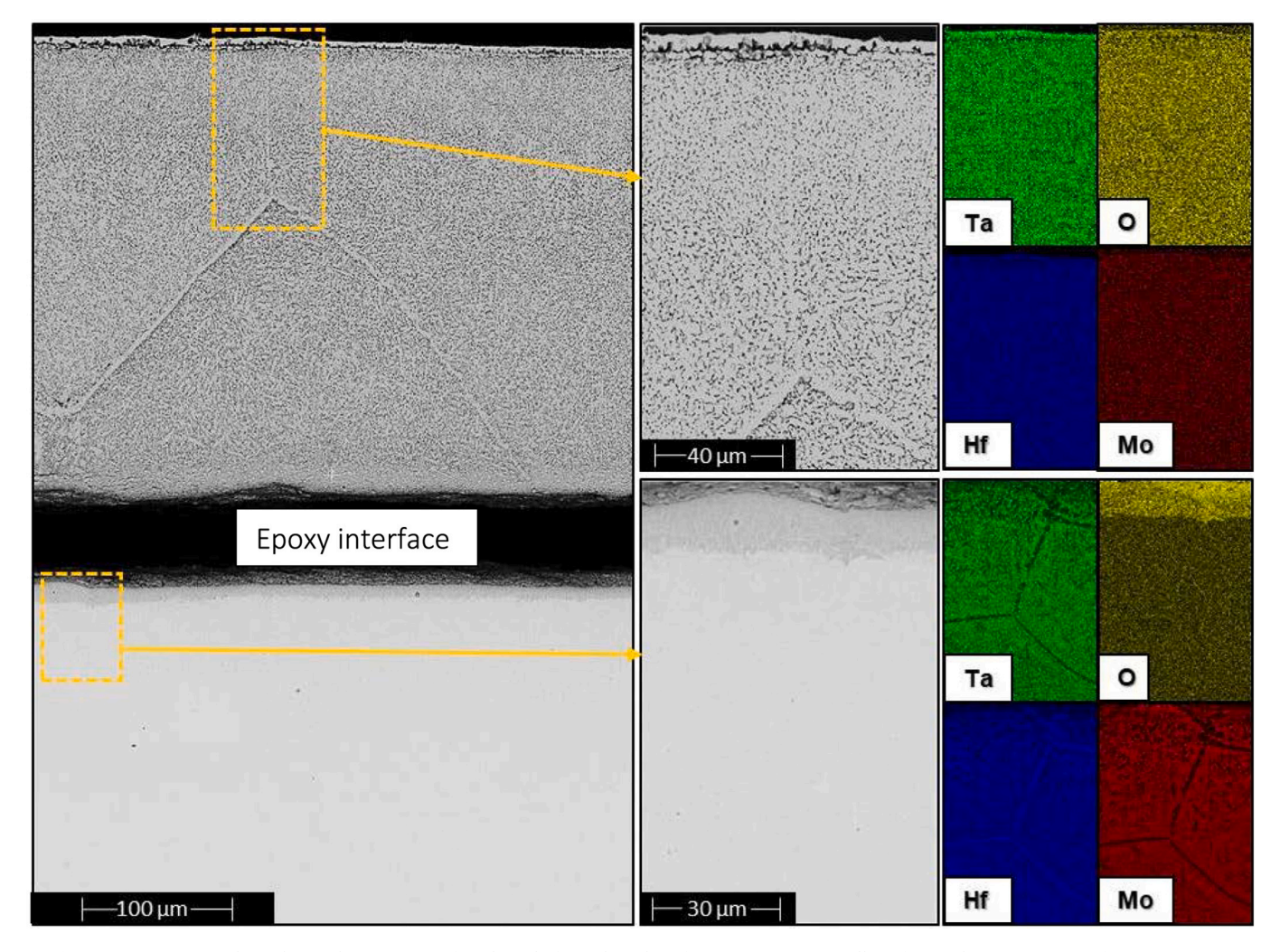


Fig. 15. BSE micrographs and EDS element maps of oxide scale formed on the Hf-21Mo-21Ta ternary alloy after oxidation at 1600 °C for 10 min in air.

comprising of a nano-lamellar mixture of the Ta-rich BCC and Hf-rich HCP phases. The phases, their volume fractions and their compositions were in good agreement with calculated phase diagrams.

Additions of Nb or Mo to the binary alloy stabilized the BCC crystal structure against transformation to the HCP structure. The microstructure of Hf-21Nb-21Ta consisted of a BCC matrix phase, spherical nanoprecipitates inside the matrix grains and two-phase BCC lamellar regions at grain boundaries. No HCP phase was detected. The two BCC phases had similar lattice parameters and were likely coherent to each other. The Hf-21Mo-21Ta alloy consisted of a BCC matrix phase and HCP precipitates.

The Hf-21Ta-21W alloy had a three-phase structure consisting of Hf-rich HCP regions, W-rich Laves phase particles and monotectoidally transformed nano-lamellar regions. The volume fractions of these constituents were estimated to be 0.4, 0.3 and 0.3, respectively. The nano-lamellar regions comprised of Ta-rich BCC and Hf-rich HCP phases.

The Calphad databases reasonably predicted the phases, volume fractions and their compositions for the binary Hf-27Ta alloy, but they failed to predict the phase contents in the studied ternary alloys. The most noticeable disagreement was for the Hf-21Nb-21Ta alloy. Although the agreements between the experimentally observed phases and calculated phase diagrams for Hf-21Mo-21Ta and Hf-21Ta-21W were

better for TCHEA-4 than for PanSolution-2020, both databases failed prediction of the phase volume fractions and compositions. Further refinement of these databases are needed.

The binary Hf-27Ta alloy had room temperature (RT) yield stress of 1708 MPa. Additions of Nb, Mo or W decreased the RT yield stress to 832 MPa, 1496 MPa or 1475 MPa, respectively. The Hf-21Mo-21Ta alloy was the strongest at $T \geq 1000~^\circ\text{C}$. It yield stress at 1000 $^\circ\text{C}$, 1200 $^\circ\text{C}$ and 1400 $^\circ\text{C}$ was 943 MPa, 421 MPa and 146 MPa, respectively.

The oxidation kinetics for Hf-27Ta, Hf-21Mo-21Ta and Hf-21Ta-21W were fairly similar and they showed mass gain of $\sim\!30\text{--}40~\text{mg/cm}^2$ during one-hour holding at 1600 °C. The Hf-21Nb-21Ta alloy exhibited much higher ($\sim\!230~\text{mg/cm}^2/\text{h})$ mass gains at 1600 °C. The resulting oxide microstructures proved to depend strongly on the alloy composition. The Hf-21Nb-21Ta and Hf-21Ta-21W alloys suffered from significant volatilization and/or melting of subsequent oxide phases, resulting in "trails" of porosity and/or entrapped material leading to the external surfaces. A similar phenomenon is believed to have occurred in the Hf-21Mo-21Ta alloy, but at a significantly faster rate, since the oxide scale exhibited fine-scale porosity and limited Mo content overall. Considering oxide morphology, mass gain and extent of cracking, the most oxidation resistant alloy was Hf-27Ta followed by Hf-21Mo-21Ta.

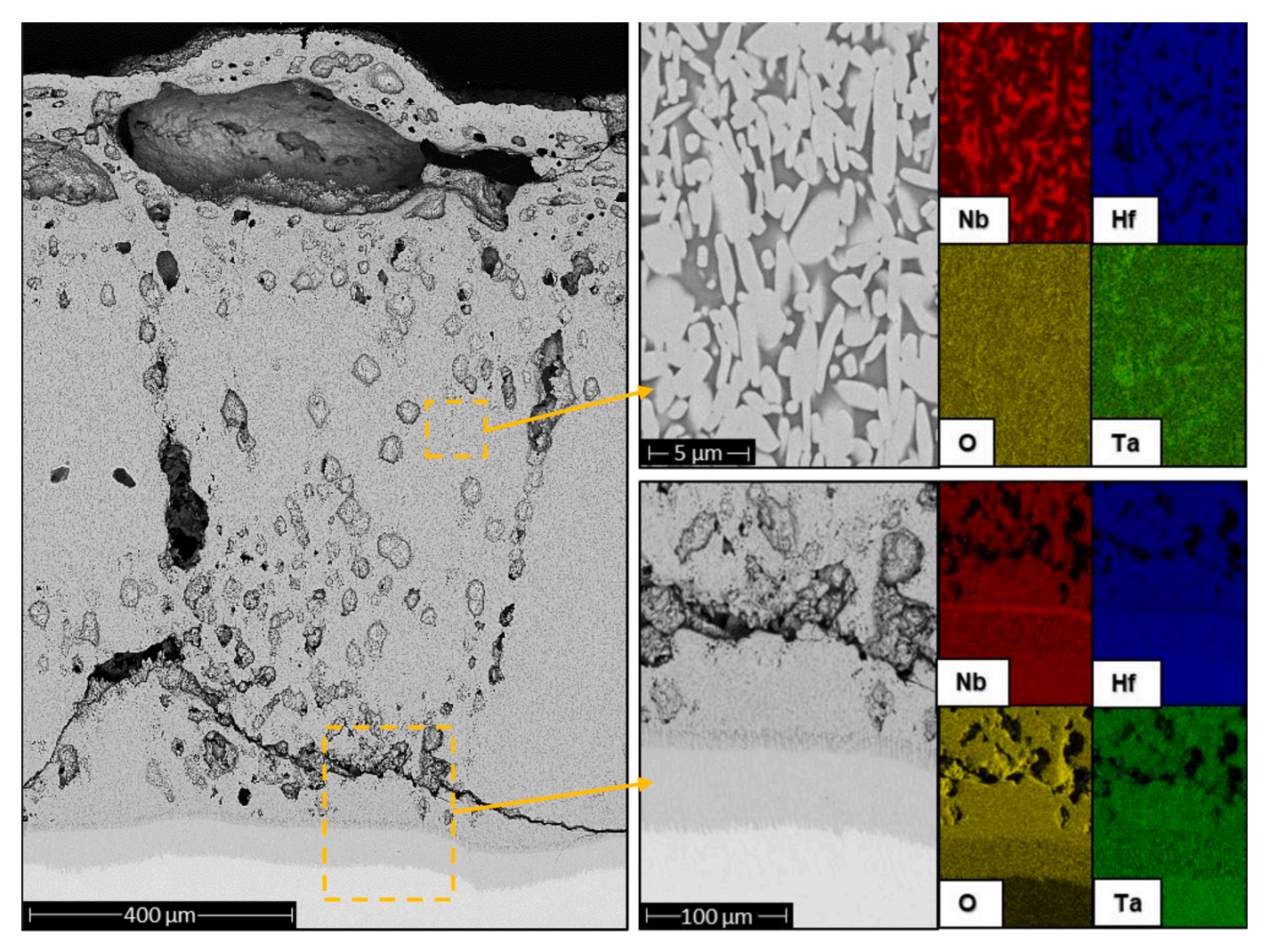


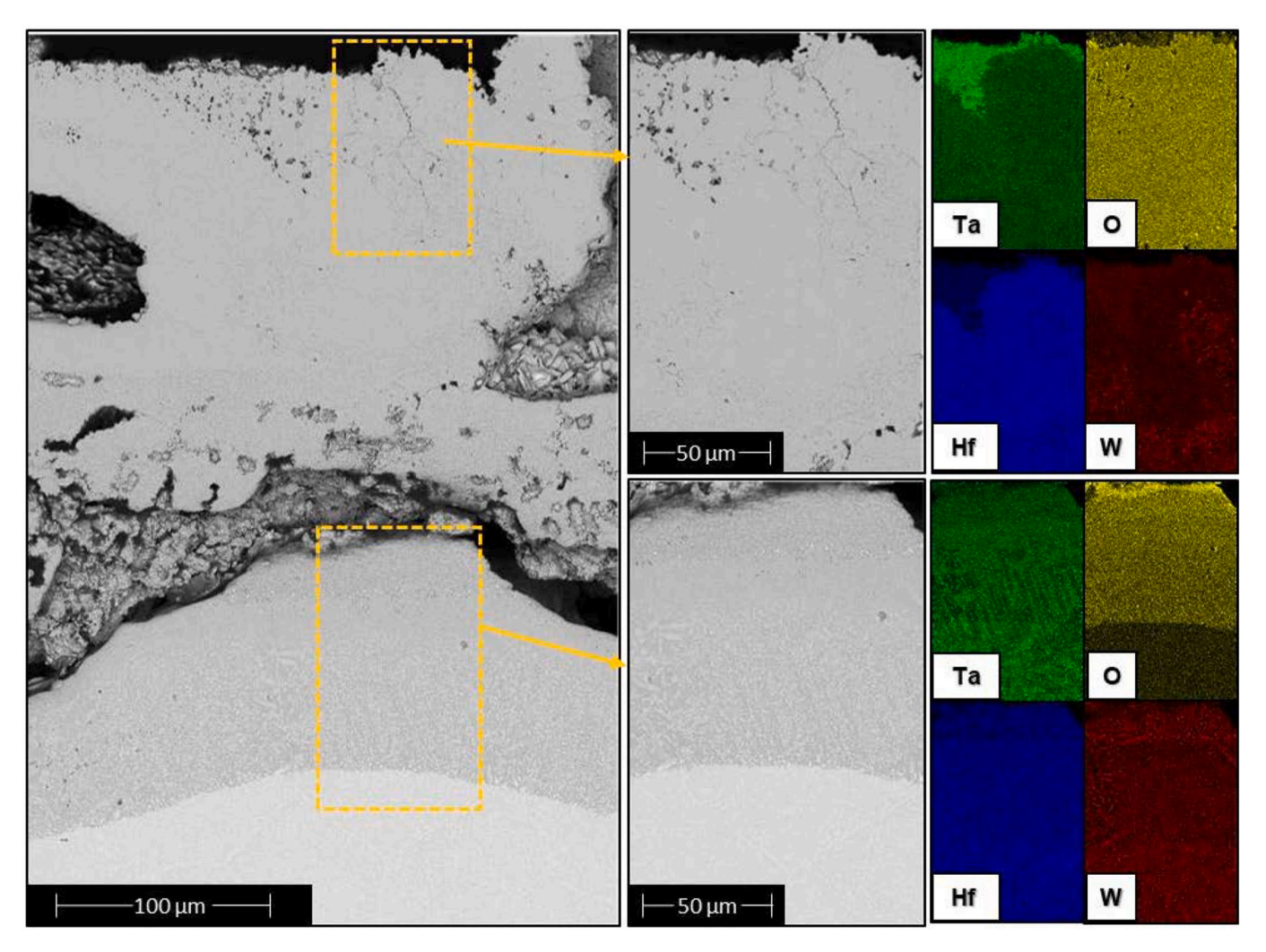
Fig. 16. BSE micrographs and EDS element maps of oxide scale formed on the Hf-21Nb-21Ta ternary alloy after oxidation at 1600 °C for 10 min in air.

Declaration of Competing Interest

The authors declare that they have no known competing financial interests or personal relationships that could have appeared to influence the work reported in this paper.

Acknowledgements

Technical assistance by M. Velez, S. Boone, L. Griffith and R. Turner is greatly appreciated. Discussions with D. Miracle, C. Woodward, S. Rao, A. Detor and S. Senkova are acknowledged. Work by ONS and TID was supported through the Air Force on-site contract FA8650-15-D-5230 managed by UES, Inc., Dayton, Ohio. MST would like to acknowledge support of the National Science Foundation, United States;



 $\textbf{Fig. 17.} \ \ \text{BSE micrographs and EDS element maps of oxide scale formed on the Hf-21Ta-21W ternary alloy after oxidation at 1600 \ ^{\circ}\text{C} \ \text{for 10 min in air.}$

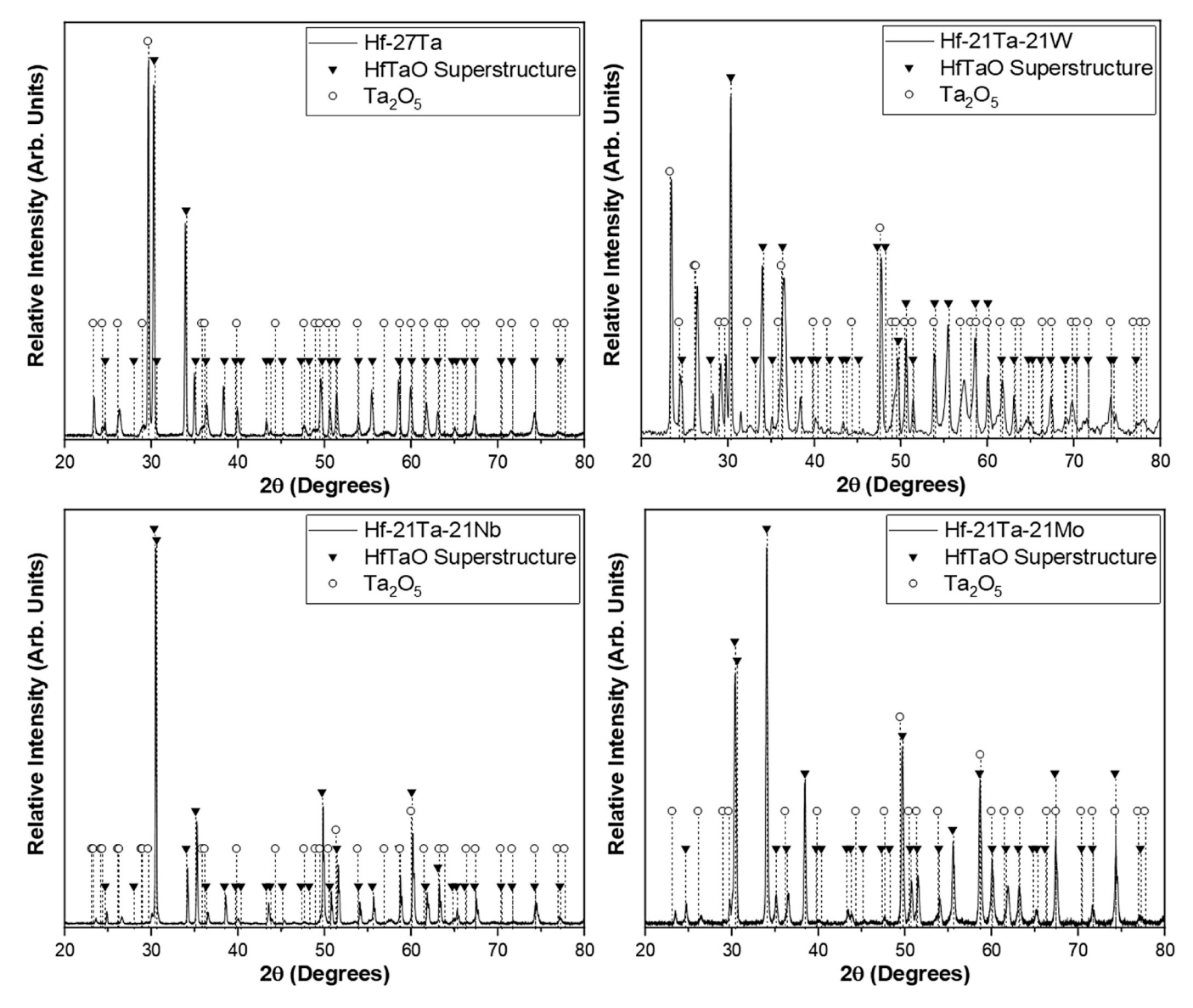


Fig. 18. X-ray diffraction patterns of oxide scales formed on the studied alloys after oxidation at 1600 °C for 10 min in air. Peaks corresponding to the orthorombic HfTaO superstructure (space group 46) and orthorhombic Ta₂O₅ (space group 74) are identified for each spectrum.

under Grant No. NSF DMREF 1922316 and an Air Force subcontract S-109-5Z6-001 managed by UES, Inc., Dayton, Ohio. The financial support of the Air Force Office of Scientific Research, Air Force Research Laboratory (AFRL), United States; and Defense Advanced Research Projects Agency (DARPA), United States is gratefully acknowledged.

References

- E. Pink, R. Eck, Refractory Metals and Their Alloys. Materials Science and Technology, WILEY-VCH Verlag GmbH, 2006, pp. 589–641.
- [2] J.H. Perepezko, The hotter the engine, the better, Science. 326 (2009) 1068-1069.
- [3] K. Marnoch, High-temperature oxidation-resistant hafnium-tantalum alloys, J. Metals 17 (1965) 1225–1231.
- [4] K. Marnoch, Some properties and applications of the hafnium-tantalum alloy, in: E.H. Beardslee (Ed.), Summary of the Thirteenth Refractory Composites Working Group Meeting, Technical Report AFML-TR-68-84. Wright-Patterson Air Force Base, Ohio, USA, Air Force Materials Laboratory, Air Force Systems Command, 1968, pp. 283–301.

- [5] J.H. Perepezko, New Oxide Materials for an Ultra High Temperature Environment. DOE Technical Report 11-13-2017-13SC005272, Department of Energy, Office of Scientific and Technical Information, USA, 2017.
- Y. Yang, J.H. Perepezko, C. Zhang, Oxidation synthesis of Hf₆Ta₂O₁₇ superstructures, Mater. Chem. Phys. 197 (2017) 154–162.
 R.A. Andrievskii, N.S. Strelnikova, N.I. Poltoratskii, E.D. Kharkhardin, V.
- [7] R.A. Andrievskii, N.S. Strelnikova, N.I. Poltoratskii, E.D. Kharkhardin, V. S. Smirnov, Melting point in systems ZrC-HfC, TaC-ZrC, TaC-HfC, in: Soviet Powder Metallurgy and Metal Ceramics 6, 1967, pp. 65–67.
 [8] V.S. Buinevich, A.A. Nepapushev, D.O. Moskovskikh, G.V. Trusov, K.V. Kuskov, S.
- [8] V.S. Buinevich, A.A. Nepapushev, D.O. Moskovskikh, G.V. Trusov, K.V. Kuskov, S. G. Vadchenko, et al., Fabrication of ultra-high-temperature nonstoichiometric hafnium carbonitride via combustion synthesis and spark plasma sintering, Ceram. Int. 46 (2020) 16068–16073.
- [9] D.L. Deadmore, Vaporization of tantalum carbide-hafnium carbide solid solutions, J. Am. Ceram. Soc. 48 (1965) 357–359.
- [10] C. Zhang, High Temperature Oxidation Study of Tantalum Carbide Hafnium Carbide Solid Solutions, PhD Thesis, Florida Interational University, Miami, Florida, USA, 2016.
- [11] S.-L. Chen, S. Daniel, F. Zhang, Y.A. Chang, X.-Y. Yanb, F.-Y. Xie, et al., The PANDAT software package and its applications, Calphad 26 (2002) 175–188.
- [12] Y.A. Chang, S.L. Chen, F. Zhang, X.Y. Yan, F.Y. Xie, R. Schmid-Fetzer, et al., Phase diagram calculation: past, present and future, in: Progress in Materials Science. 49, 2004, pp. 313–345.

- [13] J.O. Andersson, T. Helander, L. Höglund, P.F. Shi, B. Sundman, Thermo-Calc and DICTRA, Computational tools for materials science, Calphad 26 (2002) 273–312.
- [14] O.N. Senkov, S.I. Rao, T.M. Butler, K.J. Chaput, Ductile Nb alloys with reduced density and cost, J. Alloys Cmpds. 808 (2019) 151685.
- [15] H. Okamoto, Phase Diagrams for Binary Alloys, 2nd ed., ASM International, Materials Park, Ohio, 2010.
- [16] A.I. Mardare, C.C. Mardare, J.P. Kollender, S. Huber, A.W. Hassel, Basic properties mapping of anodic oxides in the hafnium-niobium-tantalum ternary system, Sci. Technol. Adv. Mater. 19 (2018) 554–568.
- [17] D.J. Young, High Temperature Oxidation and Corrosion of Metals, Elsevier, Cambridge, MA, 2016.
- [18] L. Backman, E.J. Opila, Thermodynamic assessment of the group IV, V and VI oxides for the design of oxidation resistant multi-principal component materials, J. Eur. Ceram. Soc. 39 (2019) 1796–1802.
- [19] C. Xu, W. Gao, Pilling-bedworth ratio for oxidation of alloys, Mater. Res. Innov. 3 (2000) 231–235.
- [20] S.J. McCormack, W.M. Kriven, Crystal structure solution for the $A_6B_2O_{17}$ (A = Zr, Hf; B = Nb, Ta) superstructure, Acta Crystal. Sect. B Struct. Sci. B75 (2019) 227–234.